IX. APPLIED PLASMA RESEARCH*

A. Active Plasma Systems

Academic and Research Staff

Prof. L. D. Smullin
Prof. R. J. Briggs
Prof. R. R. Parker
Prof. K. I. Thomassen

Graduate Students

Y. Ayasli
D. S. Guttman
R. K. Linford
J. A. Mangano
J. A. Rome
M. D. Simonutti

1. STABILITY OF ELECTRON BEAMS WITH VELOCITY SHEAR

We have expanded our study of cold, slab electron beams that are focused by infinite longitudinal magnetic fields to encompass the step velocity profile case. Throughout, we assume that ω_p^2 is a constant independent of the cross-sectional position x. Furthermore, we have worked in a frame of reference in which the average electron velocity is zero. The complete geometry is illustrated in Fig. IX-1.

It is obvious at the outset that this case is closely analogous to the familiar "two-stream" instability, and hence we might expect similar results. In particular, in the long-wavelength limit, with zero potential walls far from the stream edges, the potential will be essentially constant across the stream and hence the two streams will not be able "to tell" whether they are adjacent or intermixed.

This problem was studied in 1963 by Harrison and Stringer.[1] They concluded that these profiles are unstable for large enough velocity differences, but their instability conditions are quite different from ours because theirs are independent of stream width.

In general, for arbitrary velocity and density profiles, the potential is the solution of the differential equation[2]

$$\frac{d^2\phi}{dx^2} - k^2\phi + \frac{\omega_p^2(x)}{[u-v_z(x)]^2}\phi = 0, \tag{1}$$

where we assumed solutions of the form $\phi(x)\exp(i(\omega t-kz))$, and $u = \omega/k$ is the phase velocity. To test for instability, we assume that k is real and look for ω (or u) with negative imaginary parts. In each region of the beam the solution is sinusoidal, and hence we may easily derive a determinantal equation by forcing ϕ and $d\phi/dx$

*This work was supported by the National Science Foundation (Grant GK-10472).

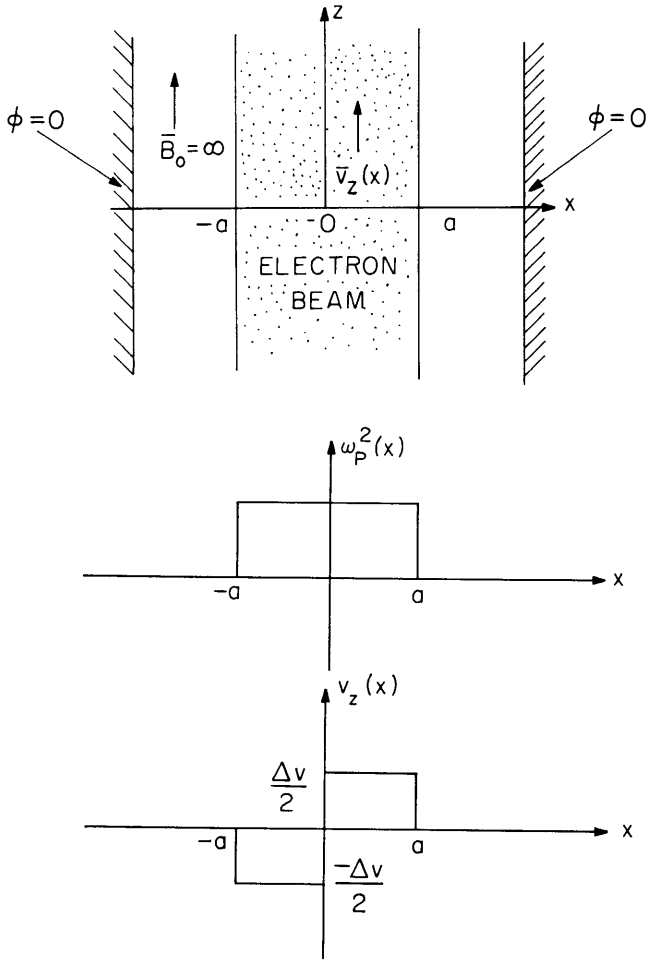

Fig. IX-1. Geometry of the step-beam.

to be continuous at the interfaces. We have found the equations for two particular cases.

I. Zero-Potential Walls at the Beam Edges

$$D(u, k) = (k_{x1}a) \cos (k_{x1}a) \sin (k_{x2}a) + (k_{x2}a) \cos (k_{x2}a) \sin (k_{x1}a). \tag{2}$$

II. Zero Potential Walls at $x = \pm\infty$

$$D(u, k) = k_{x1}a\left[(ka) \sin (k_{x2}a) + (k_{x2}a) \cos (k_{x2}a)\right]\left[(k_{x1}a) \sin (k_{x1}a) - (ka) \cos (k_{x1}a)\right]$$
$$+ k_{x2}a\left[(ka) \sin (k_{x1}a) + (k_{x1}a) \cos (k_{x1}a)\right]\left[(k_{x2}a) \sin (k_{x2}a) - (ka) \cos (k_{x2}a)\right], \tag{3}$$

where

$$k_{x1}a = \sqrt{\left(\frac{\omega_p a}{u - \left(\frac{\Delta v}{2}\right)}\right)^2 - (ka)^2}$$

$$k_{x2}a = \sqrt{\left(\frac{\omega_p a}{u + \left(\frac{\Delta v}{2}\right)}\right)^2 - (ka)^2}.$$

The roots of these equations yield the values of u and k that can exist on the beam.

The task of finding the complex roots of these equations is performed by a digital computer. Fortunately, we can prove that all of the unstable roots of D(u, k) must lie on or in the semicircle in the lower half u-plane defined by

$$\left[u_r - \tfrac{1}{2}(v_{max}+v_{min})\right]^2 + u_i^2 \leq \left[\tfrac{1}{2}(v_{max}-v_{min})\right]^2, \tag{4}$$

as is illustrated in Fig. IX-2. The minimum and maximum electron velocities in the beam are v_{min} and v_{max}. The proof of this is patterned after a similar fluid mechanics

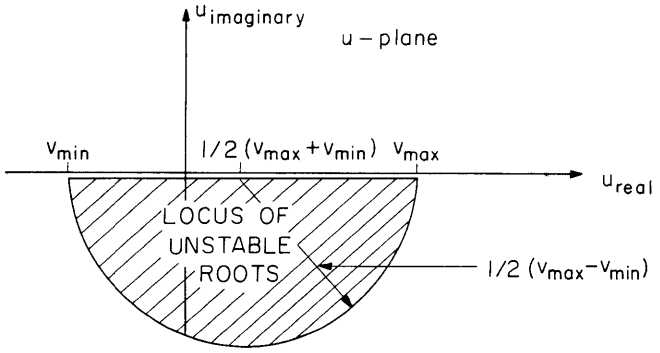

Fig. IX-2. Geometry of the semicircle theorem.

theorem.[3] It consists in multiplying Eq. 1 by ϕ^* and integrating from wall to wall. Manipulating the real and imaginary parts of the resulting equation yields the desired result.

Since the roots of D(u, k) must lie in a restricted portion of the u-plane, we can use a Cauchy integral technique to find the locations of all roots in this region. This technique, formulated by J. E. McCune and B. D. Fried,[4] uses the fact that

$$\sum_{i=1}^{N} n_i z_i^b - \sum_{j=1}^{P} p_j z_j^b = \frac{1}{2\pi i} \oint_C \frac{z^b f'(z)}{f(z)}\, dz \qquad b = 0, 1, 2, 3, \ldots < \infty, \tag{5}$$

where C is any simple, closed curve of finite length in the z-plane enclosing N zeros z_i of order n_i and P poles z_j of order p_j. For instance, if b = 0, the left-hand side of Eq. 5 yields N - P; if b = 1, it yields $\sum_i n_i z_i - \sum_j p_j z_j$, and so forth. These equations may be solved simultaneously to find the orders of the poles and zeros and their locations.

The program for calculating this complex line integral was written by James D. Callen[5] and was used successfully in the present study. As is to be expected from analogy with the two-stream situation, the onset of unstable roots occurs for the real part of u = 0. Figures IX-3 and IX-4 are plots of the imaginary part of $u/\omega_p a$ against $\Delta v/\omega_p a$. Only those roots with real (u) = 0 are shown. Also shown are the total number of roots in each range of $\Delta v/\omega_p a$, those not shown being complex and lying inside the semicircle. In Figs. IX-5 and IX-6, we show normalized ω-k diagrams for fixed $\Delta v/\omega_p a$. All modes are stabilized for large enough ka.

The case with walls at the beam edge shows a definite lower density limit below which the instability ceases. On the other hand, when the walls are moved to infinity,

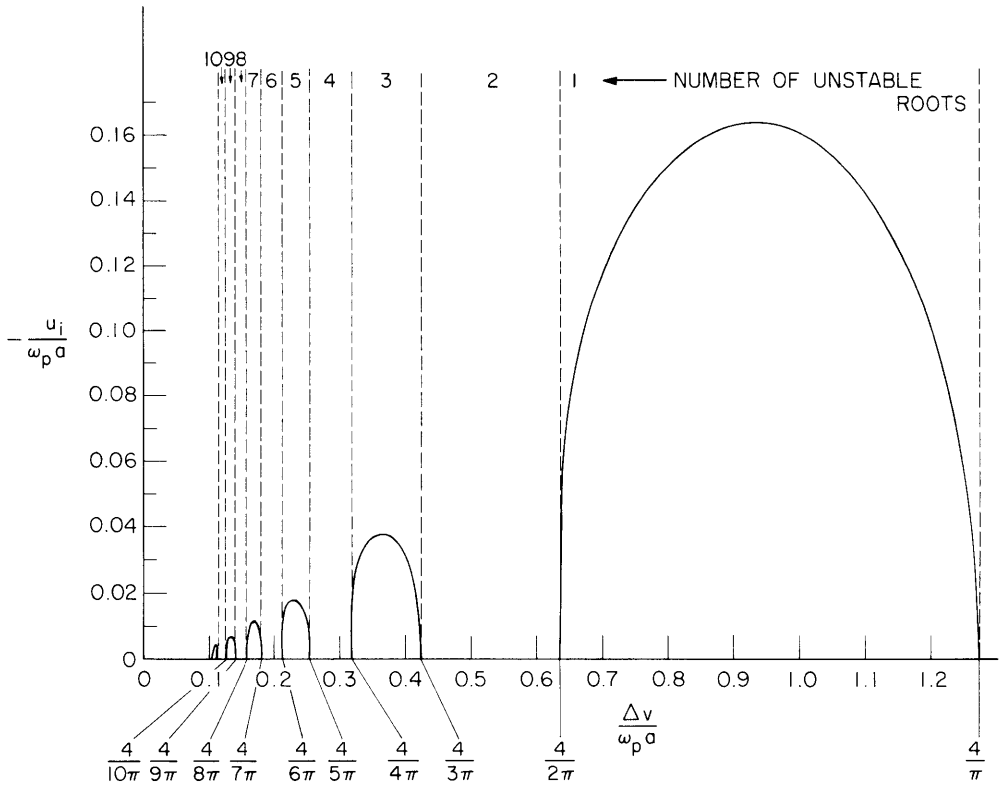

Fig. IX-3. $-u_i/\omega_p a$ vs $\Delta v/\omega_p a$ for the step beam with walls at edges for ka = 0. (Only purely imaginary roots are shown.)

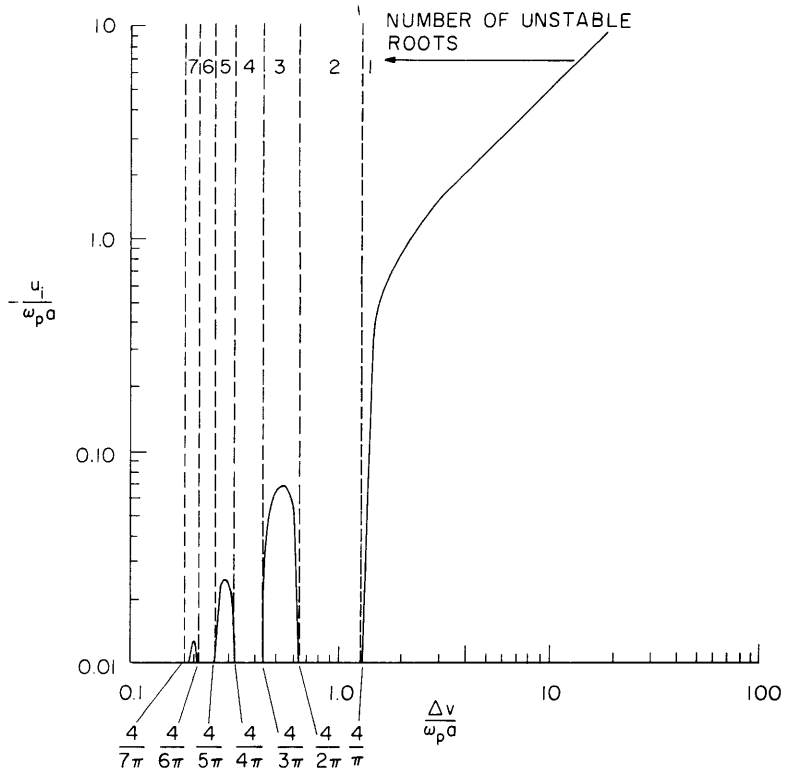

Fig. IX-4. $-u_i/\omega_p a$ vs $\Delta v/\omega_p a$ for the step beam with walls at infinity for ka = 0. (Only purely imaginary roots are shown.)

a mode persists even down to zero density for which $u_i = -\Delta v$. Figures IX-7 and IX-8 show the analogous case for the conventional interstreaming-beam situation where the number of electrons traveling at each velocity has been maintained for comparison purposes. There is fairly close agreement between the adjacent beam and interstreaming beam cases, except that the adjacent beam case has some complex roots that do not occur in the conventional two-stream case. All plots have their maximum value of $|u_i|$ when k = 0. Furthermore, as k is increased, the various modes are stabilized.

The onset of instability for each mode can easily be predicted because, for $u \equiv 0$, $k_{x1} = k_{x2} = \sqrt{\left(\frac{2\omega_p a}{\Delta v}\right)^2 - (ka)^2}$. Also, assume ka = 0. In these limits, Eqs. 2 and 3 both become

$$D(u, k) = \cos\left(\frac{2\omega_p a}{\Delta v}\right) \sin\left(\frac{2\omega_p a}{\Delta v}\right). \tag{6}$$

Thus, the neutral $k \neq 0$ modes occur when

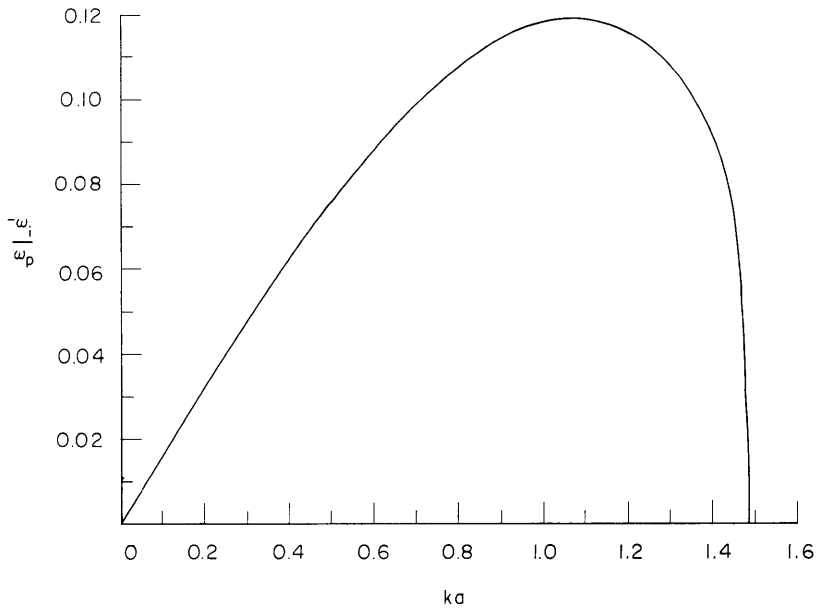

Fig. IX-5. $-\omega_i/\omega_p$ vs ka for the step beam with walls at edge for $\Delta v/\omega_p a = 0.90$.

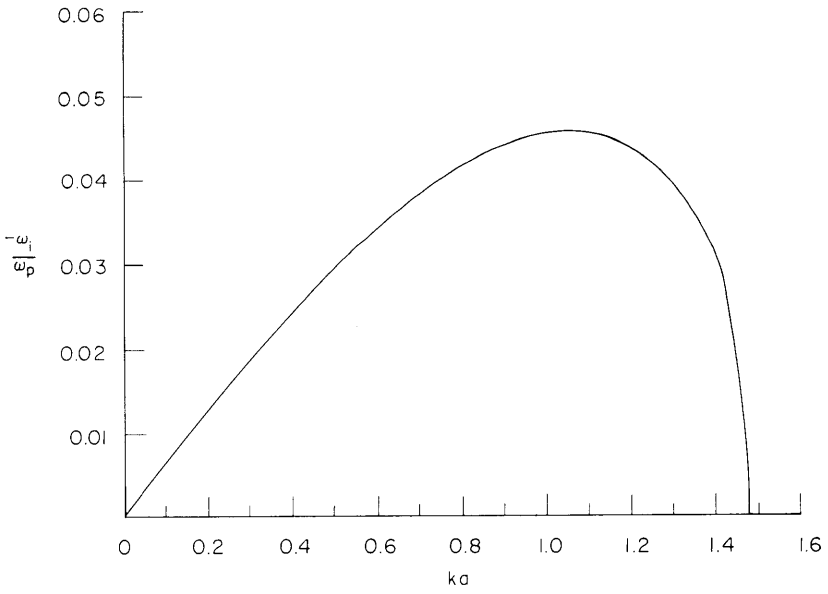

Fig. IX-6. $-\omega_i/\omega_p$ vs ka for the step beam with walls at infinity for $\Delta v/\omega_p a = 0.52$. (Only the purely imaginary root is shown.)

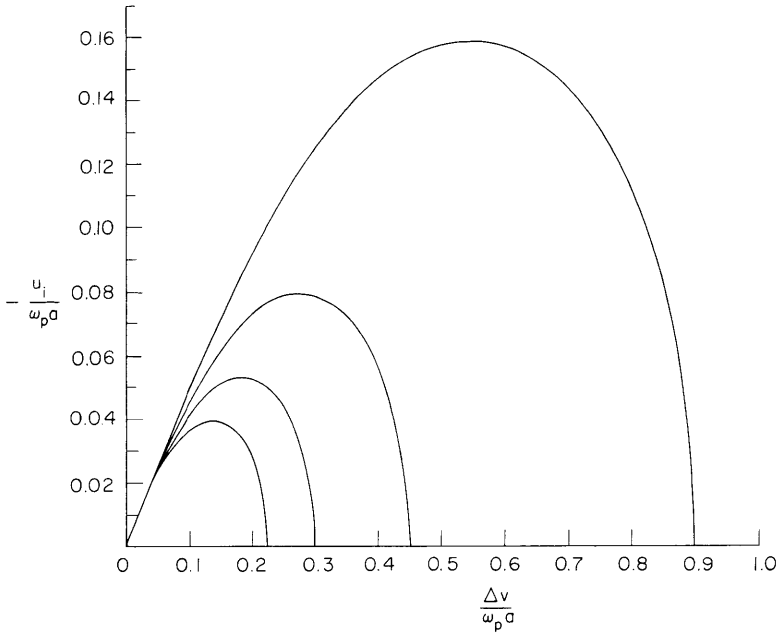

Fig. IX-7. $-u_i/\omega_p a$ vs $\Delta v/\omega_p a$ for the interstreaming beam with walls at edges for ka = 0. $u_r = (v_1+v_2)/2$.

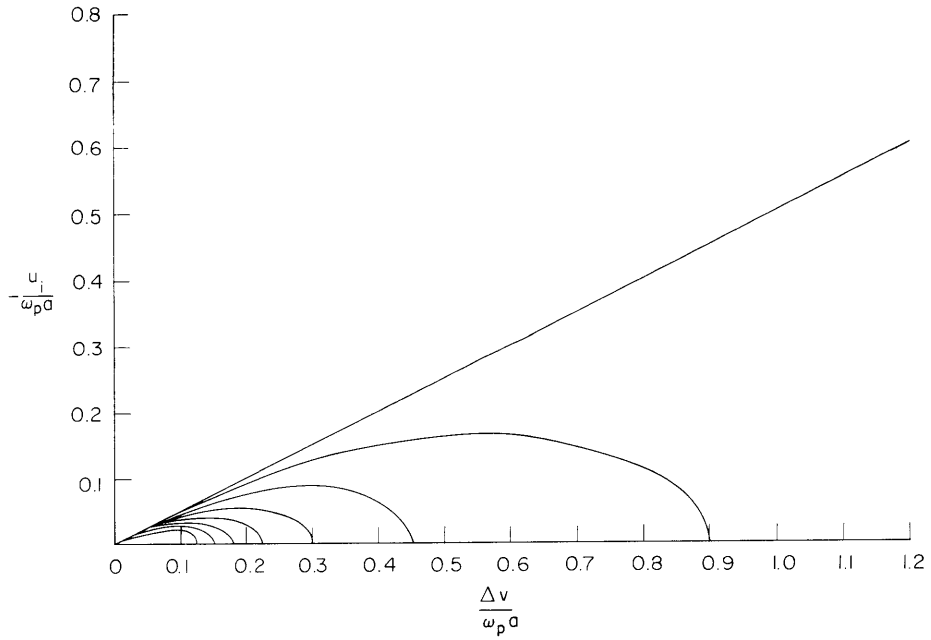

Fig. IX-8. $-u_i/\omega_p a$ vs $\Delta v/\omega_p a$ for the interstreaming beam with walls at infinity for ka = 0.

$$\frac{\Delta v}{\omega_p a} = \frac{4}{n\pi}, \qquad n = 1, 2, 3, \ldots . \tag{7}$$

In conclusion, we find that the adjacent-stream case exhibits a two-stream instability that is very similar to the conventional interspersed-stream case. When zero-potential walls are at the beam edges, there is a definite onset of instability at $\omega_p a \geq \pi\Delta v/4$. The minimum density case occurs at $k = 0$. If the walls are at infinity, there is a mode that does not exhibit a density threshold. Contrary to the interspersed case, there are complex (not pure imaginary) values of ω for real k in addition to the pure imaginary values shown here.

J. A. Rome, R. J. Briggs

References

1. E. R. Harrison and T. E. Stringer, "Longitudinal Electrostatic Oscillations in Velocity-Gradient Plasmas. II. The Adjacent-Stream Mode," Proc. Phys. Soc. (London) 82, 700 (1963).

2. R. J. Briggs and J. A. Rome, "Stability of Electron Beams with Velocity Shear," Quarterly Progress Report No. 90, Research Laboratory of Electronics, M.I.T., July 15, 1968, pp. 106-107.

3. P. G. Drazin and L. N. Howard, "Hydrodynamic Stability of Parallel Flow of Inviscid Fluid," Advances in Applied Mechanics 9, 62 (1966).

4. J. E. McCune and B. D. Fried, "The Cauchy-Integral Root-Finding Method and the Plasma 'Loss-Cone' Instability," Report CSR TR-67-1, Center for Space Research, M.I.T., January 1967.

5. J. D. Callen, "Absolute and Convective Microinstabilities of a Magnetized Plasma," Report CSR TR-68-3, Center for Space Research, M.I.T., April 1968.

IX. APPLIED PLASMA RESEARCH*

B. Plasma Effects in Solids

Academic and Research Staff

Prof. A. Bers
Prof. G. Bekefi
Dr. E. V. George

Graduate Students

R. N. Wallace

1. MODEL FOR THE MICROWAVE EMISSION FROM THE BULK OF n-TYPE InSb

Our recent experiments on the microwave noise emission from the bulk of n-type InSb at 77°K in applied crossed electric and magnetic fields show two important features[1]: (a) the emission originates from localized regions of the material; and (b) the thresholds of electric and magnetic fields are higher than those found in samples with "bad" contacts.[2] From these results, we conjecture that the emission is related to inhomogeneities in the material. Metallurgical studies[3] show that in most InSb crystals inhomogeneities in the impurity density occur in 1-10 μ regions. The detailed nature of these inhomogeneities is unknown, but it is clear that the electric field in regions of lower electron density would be higher (perhaps by a factor of 2-4) than the average applied field. Furthermore, as we shall show, in the presence of a transverse magnetic field the rate at which electrons gain energy from the electric field is also enhanced. Taken together, these two effects predict that a fraction of the current will produce charge multiplication in localized regions, and we can compute the resultant shot-noise generated. We shall summarize the analytical results of this model and compare them with our observations.

Energy Gained by Electrons in Crossed Electric and Magnetic Fields

This problem has been treated in the past phenomenologically for predicting total-current breakdown in a strong Hall electric field.[4] Our interest is in a more detailed description of the electron energy gained from the total electric field (applied field and Hall field), since only a small fraction of the current is considered to produce breakdown. Hence we start with the time-independent Boltzmann equation for the electron distribution function $f(\bar{v}, \bar{E}, \bar{B})$ in electric and magnetic fields $\bar{E}$ and $\bar{B}$,

*This work was supported by the National Science Foundation (Grant GK-10472).

$$\frac{e}{m^*(\epsilon)} (\bar{E} + \bar{v} \times \bar{B}) \cdot \nabla_{\bar{v}} f = - \frac{f}{\tau(\epsilon)}, \tag{1}$$

where we have assumed a relaxation-time approximation for the collisions and (ϵ) energy-dependent effective mass m^* and relaxation time τ. We separate f into its isotropic and anisotropic parts

$$f = f_i + f_a \tag{2}$$

from which the current is given by

$$\bar{J} = en \frac{\sum_v f_a \bar{v}}{\sum_v f_i}, \tag{3}$$

where n is the electron density. Substituting Eq. 2 in Eq. 1, we can solve for f_a in terms[5] of f_i

$$f_a = -e\tau \frac{df_i}{d\epsilon} \bar{v} \cdot \frac{(\bar{E} + \tau \bar{\omega}_c \times \bar{E})}{\left(1 + \omega_c^2 \tau^2\right)}, \tag{4}$$

where we have assumed that $\bar{E}$ is perpendicular to $\bar{B}$ and the anisotropic part of $(\bar{E} \cdot \nabla_v f_a)$ is negligible,[5] and have written $\bar{\omega}_c = \bar{B}e/m^*$. Using Eq. 4 in Eq. 3, and letting $\bar{B} = \bar{i}_z B_o$, $\bar{E} = \bar{i}_x E_x + \bar{i}_y E_y$, we find

$$J_x = e^2 n \left[\left\langle \frac{\tau/m}{1 + \omega_c^2 \tau^2} \right\rangle E_x - \left\langle \frac{\omega_c \tau^2/m}{1 + \omega_c^2 \tau^2} \right\rangle E_y \right] \tag{5}$$

$$J_y = e^2 n \left[\left\langle \frac{\omega_c \tau^2/m}{1 + \omega_c^2 \tau^2} \right\rangle E_x + \left\langle \frac{\tau/m}{1 + \omega_c^2 \tau^2} \right\rangle E_y \right], \tag{6}$$

where the brackets indicate the following average over the energy distribution function

$$\langle X \rangle = \frac{\sum_\epsilon \left(-\frac{2}{3} \epsilon \frac{df_i}{d\epsilon} X \right)}{\sum_\epsilon f_i}. \tag{7}$$

Consider now that the applied electric field E_o is in the x direction, and the geometry is one of zero Hall current, $J_y = 0$. The Hall electric field is then given by

$$E_y = -\frac{\left\langle \frac{\omega_c \tau^2/m}{1+\omega_c^2\tau^2} \right\rangle}{\left\langle \frac{\tau/m}{1+\omega_c^2\tau^2} \right\rangle} E_x$$

$$\equiv -\phi_H E_o. \tag{8}$$

Our interest is to determine the energy gained by an electron of a particular energy from both the applied and Hall electric fields. The "drift" velocity of an electron of a particular energy, $v(\epsilon)$, may be found from Eqs. 5 and 6 by dividing them by (en) and removing the brackets. Then, using Eq. 8 for E_y, the power input to an electron of a particular energy is

$$P_I(\epsilon) \equiv e\,\bar{v}(\epsilon)\cdot\bar{E}$$

$$= \frac{e^2\tau}{m^*}\,\frac{1+\phi_H^2}{1+\omega_c^2\tau^2}\,E_o^2, \tag{9}$$

where τ and m^* are energy-dependent.

Charge-Multiplication and Shot-Noise Generation

In order to determine the conditions for the onset of local breakdown, we must compare the energy-gain rate of Eq. 9 with the energy-loss rate. The energy-loss rate to optical phonons is given by $\hbar\omega_o/\tau_e$, where ω_o is the optical phonon frequency, and τ_e is the electron energy relaxation time. An electron starting from an energy ϵ may gain energy and produce an ionizing collision, provided P_I exceeds $\hbar\omega_o/\tau_e$ for energies from ϵ to above the energy gap ϵ_g.

Figure IX-9 is a plot of the normalized energy gain and loss rates, P_I/E^2 and $\hbar\omega_o/\tau_e E^2$, as a function of electron energy. In making this plot, we have used known data for the variation of the effective mass with energy,[6] and theoretical formulas for the electron momentum and energy scattering times in interactions with optical phoons.[7] An average momentum scattering time of 4×10^{-12} s, deduced from the low-field electron mobility, was used for electron energies less than $\hbar\omega_o$. We note that for sufficiently small values of E and B_o no electrons satisfy the condition $P_I > \hbar\omega_o/\tau_e$. As E and B_o are increased, P_I eventually exceeds $\hbar\omega_o/\tau_e$ for energies from some value $\epsilon_a < \epsilon_g$ through energies above ϵ_g. The fraction of the electrons having energy greater than ϵ_a can gain energy from the total electric field to produce ionizing collisions. This

"ionizing fraction," F, of the electron population can be computed by assuming an appropriate Maxwellian distribution, which we shall describe.

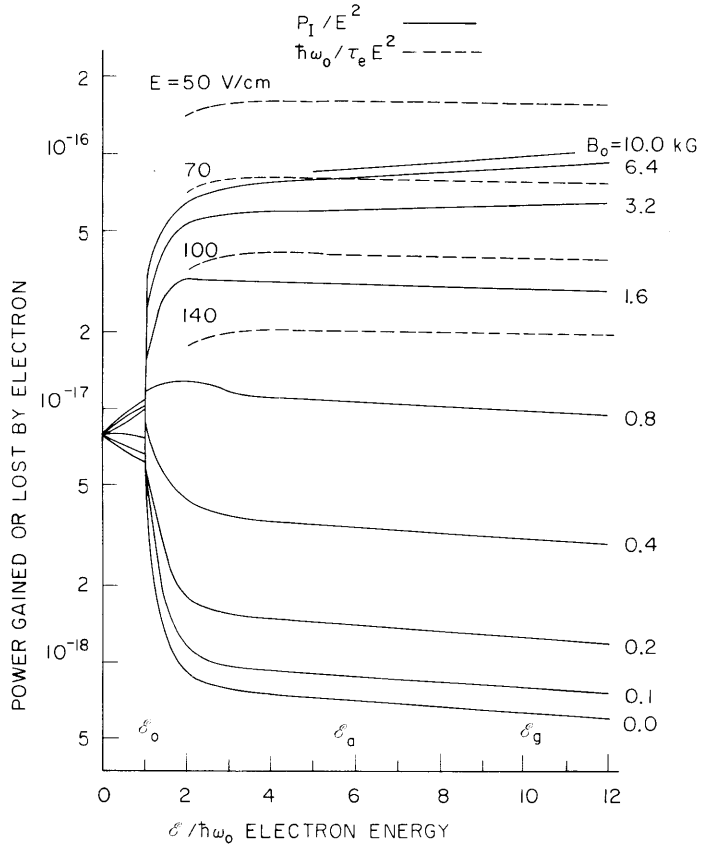

Fig. IX-9. Normalized energy gain and loss rates per electron as a function of the electron energy in optical phonon units for various values of E and B_o. (E is the local value of the applied electric field.)

The conditions in a typical inhomogeneity region of an InSb crystal are then considered. From the known order of length of the inhomogeneity region we find that each electron in the "ionizing fraction" creates, on the average, one additional electron-hole pair. These generated carriers give rise to a shot-noise-producing current which is approximately FI_o, where I_o is the drift current in the sample.[8] The inhomogeneity region can then be thought of as a localized microwave current source of rms value $[2eFI_o(\Delta f)]^{1/2}$, where Δf is the receiver bandwidth. In our experiments,[1] this localized current source, together with the loop sample forms a driven antenna system that excites the eccentric transmission line. The power coupled from this "antenna" to the eccentric transmission line can then be computed directly.

Comparison with Experiment

The power delivered to the receiver is proportional to $\left|\int \bar{h}_T \cdot \bar{J}_a \, dA\right|^2$, where $\bar{h}_T$ is the magnetic field mode function for our eccentric transmission line, A is the cross section of the line, and $\bar{J}_a$ is the microwave current density distribution on the loop sample as determined above. From this, we can calculate the output power as a function of sample rotation and compare with our experimental results.[1] This is shown in Fig. IX-10 for a sample that showed a marked variation in output with sample rotation.

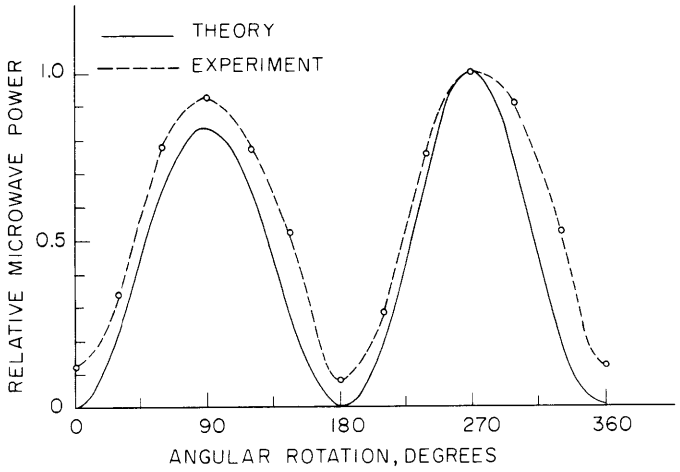

Fig. IX-10. Comparison of theoretical and experimental variation of microwave power with sample rotation, with B_o perpendicular to the sample plane. Frequency = 9 GHz.

We conclude that our model of a localized source is indeed supported by experiment.

We next turn to a more detailed test of our model in which we seek to predict the observed E_o-B_o threshold curve and the output power at threshold (Fig. IX-11). The two principal unknowns in our model are the electric field in the inhomogeneity region (which may be M times larger than the nominal applied field E_o) and the electron energy distribution function. The first affects the actual electric field (Eq. 9) and the second enters into ϕ_H, both then determining ϵ_a (Fig. IX-9) and thus the B_o vs E_o dependence of the ionizing fraction F. We shall initially assume that M is in the range 2-4, and that the electron distribution function is a two-temperature Maxwellian with different temperatures above and below the optical phonon energy.[9] The electrons in the main body of the distribution ($\epsilon < \hbar\omega_o$) essentially determine ϕ_H, while the electrons in the high-energy tail ($\epsilon > \hbar\omega_o$) will affect the detailed magnitude of F. When acoustic phonon scattering determines the main body of the distribution function, it can be shown[5] that

in moderately high electric and magnetic fields ($\mu E/v_a \gg \omega_c \tau_a \gg 1$, where v_a and τ_a are the acoustic velocity and scattering time) the isotropic part of this distribution, f_1, is

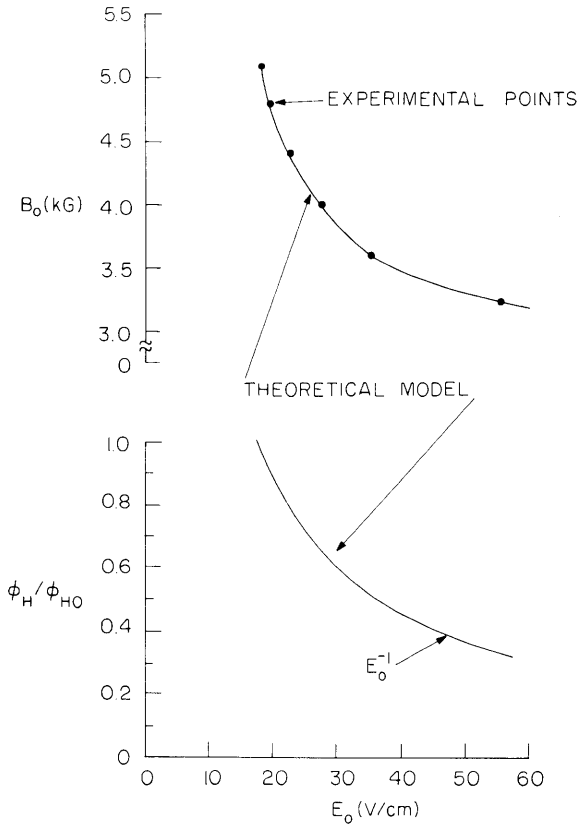

Fig. IX-11. Experimental values (dots) of electric and magnetic field required to maintain a constant threshold (minimum detectable) emission level equivalent to that of a thermal source of $0.5\text{-}1.0 \times 10^3$ °K at 9.0 GHz. The theoretical model with $\phi_H \sim E_o^{-1}$ predicts the observed threshold fields and gives the observed emission power level if the electron distribution tail temperature varies as E_o.

approximately Maxwellian with an electron temperature that increases as E_o^2. Adopting this for electrons below the optical phonon energy leads to $\phi_H \sim E_o^{-1}$. We can then determine the tail temperature which gives the output power level observed on the threshold curve (Fig. IX-11). We find a tail temperature that increases approximately as E_o, and hence remains at a lower temperature than the main body of electrons.[10] Our calculations show that the predicted threshold field variation is essentially the same for a range of $M\phi_{Ho}$,[11] where $\phi_{Ho} = \phi_H$ ($E_o \approx 0$), and hence the precise value of M need not be

known. Further knowledge of the electron distribution function with applied fields would, however, provide additional means for testing our model.

A. Bers, R. N. Wallace

References

1. R. N. Wallace, Quarterly Progress Report No. 96, Research Laboratory of Electronics, M.I.T., January 15, 1970, p. 131.
2. E. V. George, Quarterly Progress Report No. 96, Research Laboratory of Electronics, M.I.T., January 15, 1970, p. 129.
3. A. F. Witt and H. C. Gatos, J. Electrochem. Soc. 113, 808 (1966); A. F. Witt, idem 114, 298 (1967).
4. M. Toda and M. Glicksman, Phys. Rev. 140, A1317 (1965).
5. H. F. Budd, Phys. Rev. 131, 1520 (1963).
6. F. R. Kessler and E. Sutter, Z. Naturforsch. 16a, 1173 (1961).
7. E. M. Conwell, High Field Transport in Semiconductors (Academic Press, Inc., New York, 1967), pp. 157-158.
8. The transit time of the electrons through the field-enhanced regions is small enough to insure a flat shot-noise spectrum throughout the range of observed microwave frequencies.
9. Such a distribution function has been used for InSb in a different context by G. Perskey and D. J. Bartelink, I.B.M. J. Res. Develop. 13, 607 (1969).
10. Calculations based on a single-temperature Maxwellian with $T_e \sim E_o^2$ predict a threshold-field curve that is very close to the observed one. A separate tail temperature variation is only required for an exact fit to the output power level.
11. $\phi_{Ho} \approx \mu B_o$, and μ is in the range $5\text{-}7 \times 10^5$ cm^2/V-sec; in addition, requiring that $\hbar\omega_o < \epsilon_a < \epsilon_g$ for our threshold fields allows us to range M from 3 to 4.

IX. APPLIED PLASMA RESEARCH*

C. Plasma Physics and Engineering

Academic and Research Staff

Prof. R. A. Blanken
Prof. T. H. Dupree
Prof. E. P. Gyftopoulos
Prof. L. M. Lidsky
Prof. W. M. Manheimer
Dr. E. Oktay

Graduate Students

D. P. Hutchinson
M. A. Lecomte
C. A. Primmerman
A. S. Ratner
J. E. Robinson
C. E. Wagner

1. ELECTRON CYCLOTRON RESONANCE HEATED PLASMA IN A LEVITRON

We shall report on an investigation of the stability of an electron cyclotron resonance heated plasma in a levitron, shown schematically in Fig. IX-12. Heating was accomplished with a 1-MW, 10-μs pulse of microwaves with frequency approximately 2.8 GHz (S-band). The poloidal magnetic field was produced by discharging a capacitor bank into a circular coil, which entered the chamber through port N2. The toroidal field was created by discharging a capacitor bank through several turns of wire inside a longitudinal

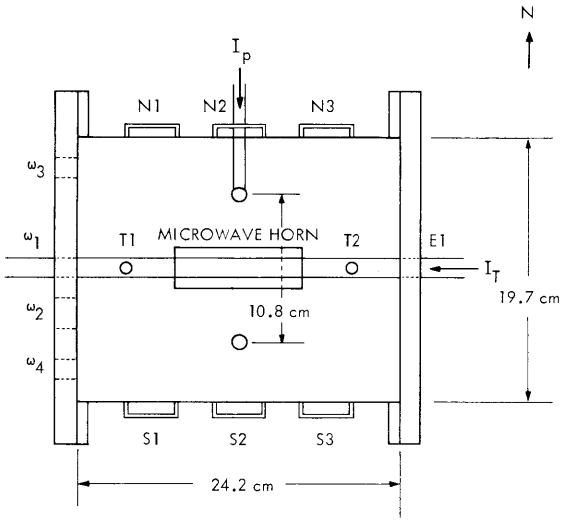

Fig. IX-12. Schematic of the levitron showing labeling of ports.

bar that entered at ports E1 and W1 and passed perpendicularly through the center of the coil. The toroidal field affected the shear, or twist, of the magnetic field lines. Electron-cyclotron heating occurred on a range of surfaces about the 1-kG surface, which formed a torus around the poloidal magnet. The diagnostics utilized included a

*This work is supported by the National Science Foundation (Grant GK-10472).

phototube, single and double probes, and 8 wall-loss probes situated symmetrically in the plane of the poloidal coil, 1.0 cm off the wall, as shown in Fig. IX-13.

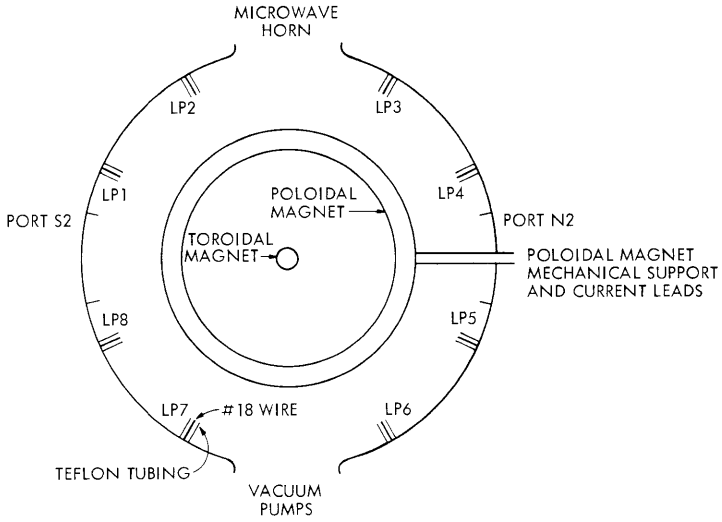

Fig. IX-13. Positioning and labeling of wall-loss probes.

The magnetic configuration of the levitron was proposed by Lehnert, in 1958.[1] Levitron experiments, principally at the Lawrence Radiation Laboratory[2] and at the Culham Laboratory,[3] have produced plasmas with densities of from 10^{10} to 10^{12} cm^{-3}, with electron temperatures of 1-30 eV, and with energy decay times typically of 5-30 times the Bohm time. A similar device, the spherator,[4] is in operation at the Plasma Physics Laboratory, Princeton University.

Basic Plasma Properties

a. Microwave Heating

The microwaves were triggered at the peak of the magnetic current. The magnetic field decayed approximately 4% during the lifetime of the plasma. The 10-μs microwave pulse ionized and heated the gas in the chamber, typically Hydrogen or Argon at pressures of $\sim 10^{-5}$ Torr. The dispersion relation for electromagnetic waves propagating in a plasma in the absence of a magnetic field predicts total reflection of the microwaves when the gas has been ionized to the extent that the electron density is such that the plasma frequency exceeds the microwave frequency. This corresponds to a density of 9×10^{10} cm^{-3}. This dispersion relation was modified by the presence of the magnetic field and by the geometry of the levitron. The reflection phenomena was qualitatively observed on the reverse microwave power monitor.

b. Nature of the Plasma

The light output of the plasma, which could be observed with the naked eye, was measured with a phototube. Figure IX-14a shows the phototube output for a Hydrogen plasma with a neutral-particle pressure of 4.3×10^{-5} Torr. There are three discernible peaks: at t = 2, 7, and 12 μs. Time is measured from the start of the microwave pulse. Figure IX-14b shows the output for a hydrogen plasma with a neutral-particle pressure

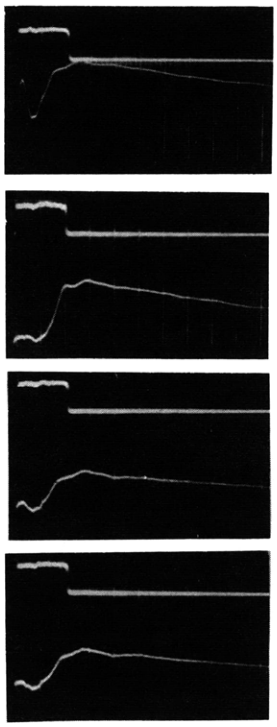

Fig. IX-14.

Phototube output. The upper trace is the microwave pulse. Horizontal scale: 5 μs/div. I_p = 6000 A. I_t = 1000 A. (a) Hydrogen, 4.3×10^{-5} Torr. (b) Hydrogen, 8.6×10^{-6} Torr. (c) Argon, 4.2×10^{-5} Torr. (d) Argon, 8.4×10^{-6} Torr.

of 8.6×10^{-6} Torr, with peaks at t = 2, 10, and 15 μs. The first peak corresponds to the breakdown of the hydrogen. The later peaks are probably the result of ionizations caused by collisions between electrons heated by cyclotron resonance and neutrals. Figure IX-14c and IX-14d shows the phototube output for an Argon plasma with neutral-particle pressures of 4.2×10^{-5} and 8.4×10^{-6} Torr, respectively. The breakdown peak at t = 2 μs is less prominent than with hydrogen. The later peaks are at t = 9, 14, and 25 μs.

The plasma density and electron temperature were measured by using standard electrostatic and double floating probe techniques. The density measurements were corrected for electron Debye length effects with the method of Laframboise.[5] The electron temperature of the Hydrogen plasma of neutral-particle pressure of $\sim 4\text{-}6 \times 10^{-5}$ Torr was measured to be 30-70 eV at densities of $\sim 1 \times 10^{10}$ cm^{-3} immediately after the end

of heating. At a neutral-particle pressure of $\sim 9 \times 10^{-6}$ Torr, the electron temperature was 120 eV at densities of 1×10^{10} cm^3. This represents 2% ionization. Argon plasmas were hotter and denser. An electron temperature of 100 eV and density of $\sim 1 \times 10^{11}$ cm^{-3} at t = 20 μs were achieved at a neutral-particle pressure of 4×10^{-5} Torr. At a neutral pressure of 8×10^{-6} Torr, the electron temperature was 135 eV at $\sim 1 \times 10^{11}$ cm^{-3}.

Several density profiles were measured. Figure IX-15 shows a density profile measured from the toroidal magnet out to the inner radius of the poloidal magnet, and from the outer radius of the poloidal magnet to the wall-loss probes that were grounded to act as limiters. The longitudinal profile was measured from the surface of the poloidal

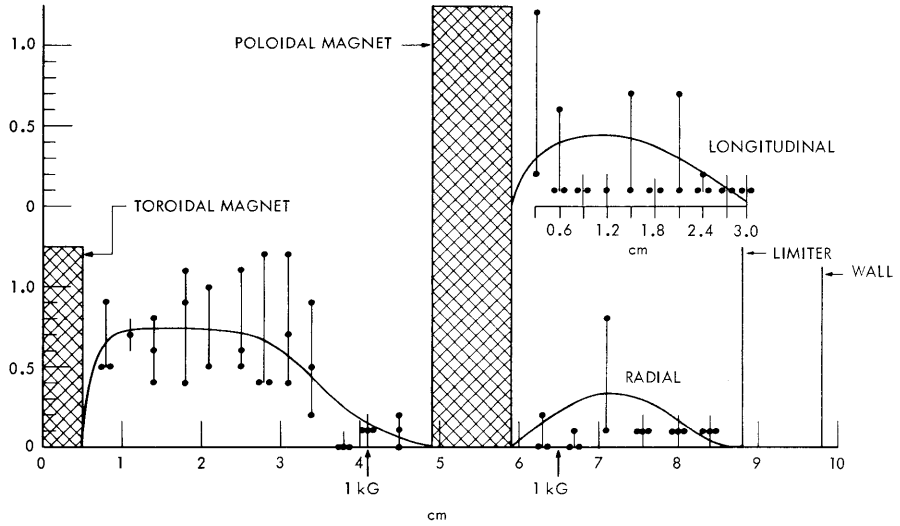

Fig. IX-15. Radial and longitudinal density profile. Hydrogen, 4.3×10^{-5} Torr. I_p = 6000 A. I_t = 1000 A. t = 15 μs.

magnet outward in a direction perpendicular to the plane of the poloidal magnet. The density gradients were observed to be of the order of 1 cm near the poloidal magnet, and 0.5 cm near the toroidal magnet.

The plasma floating potential was measured with a high input impedance, wide-bandwidth amplifier. For a Hydrogen plasma with a neutral-particle pressure of 4.3×10^{-5} Torr, the floating potential within the poloidal coil typically rose to 15 V positive at t = 6-8 μs as electrons were lost. As the electron loss rate changed, the floating potential declined to 10-15 V negative at t = 15 μs, and then decayed to zero. At the wall-loss probes, the floating potential typically rose to 8 V positive at t = 1 μs, dropped to 5 V negative at t = 2 μs, rose to 10 V positive at t = 6 μs, and then decayed to zero with a time constant of 40-60 μs.

Experimental Observations

a. Asymmetries

Asymmetries were noted in the plasma floating potential and plasma density in the vicinity of the poloidal coil support. The ion saturation current was measured using the wall-loss probes, and found to be isotropic except at the probes just above (LP4) and below (LP5) the poloidal support. At a neutral-particle pressure of 4.3×10^{-5} Torr of Hydrogen and at high values of shear, the plasma density was higher above the support and lower below the support than that measured at the other wall-loss probes. The density ratio of above the support to below the support was 1.8. At lower values of shear, the density above the support decreased, though it was still above normal, while the density below the support increased to values above normal. The density ratio declined to 1.1. Figure IX-16 shows the ion saturation current as measured at the LP2, LP4, and LP5 wall-loss probes. The floating potential was significantly higher as measured with LP4 than with LP5, as shown in Fig. IX-16b. The potential at LP5 was essentially the same as that measured at the probes far from the support. The potential at LP4 remains at 15 V positive from $t = 15$ to $t = 45$ μs. This is 5-10 V higher than at LP5. The floating potential at LP3 was similar to that at LP4, thereby indicating that the extent of the potential perturbation was ~10 cm above the support.

Insertion of a Langmuir probe through port S2 was observed to reduce the floating potential by approximately 20% at LP1 and to have no effect on LP8.

The presence of the poloidal support could have caused a density gradient along magnetic field lines. As the isobaric surfaces would no longer coincide with the magnetic surfaces, an electric field could exist. The $\underline{E} \times \underline{B}$ drift can result in plasma loss across magnetic field lines. This phenomenon is known as convective cell loss.[4, 6-9]

b. Oscillations

The levitron plasma was free of large-amplitude oscillations. The normalized amplitude was generally well under 10%, except during microwave heating, when the single-probe measurements oscillated violently. Figure IX-17a shows ion saturation current inside of the poloidal coil. The oscillations during heating were ~1 MHz.

Oscillations were observed in the afterglow using the double floating probe. Figure IX-17b and IX-17c shows the probe current for bias voltage of 10 and 30 V, respectively, at a neutral pressure of 4.3×10^{-5} Torr of Hydrogen. The oscillations were 300-500 kHz. Figure IX-17d shows the probe current for a bias voltage of 60 V at a neutral pressure of 4.2×10^{-5} Torr of Argon. The oscillations were 800-1000 kHz. The double probe was situated within the poloidal ring, 1.0 cm from the coil surface.

These oscillations in the afterglow could not be explained by cyclotron waves. The ion-cyclotron frequencies were typically ~500-2000 kHz for Hydrogen and 10-60 kHz for

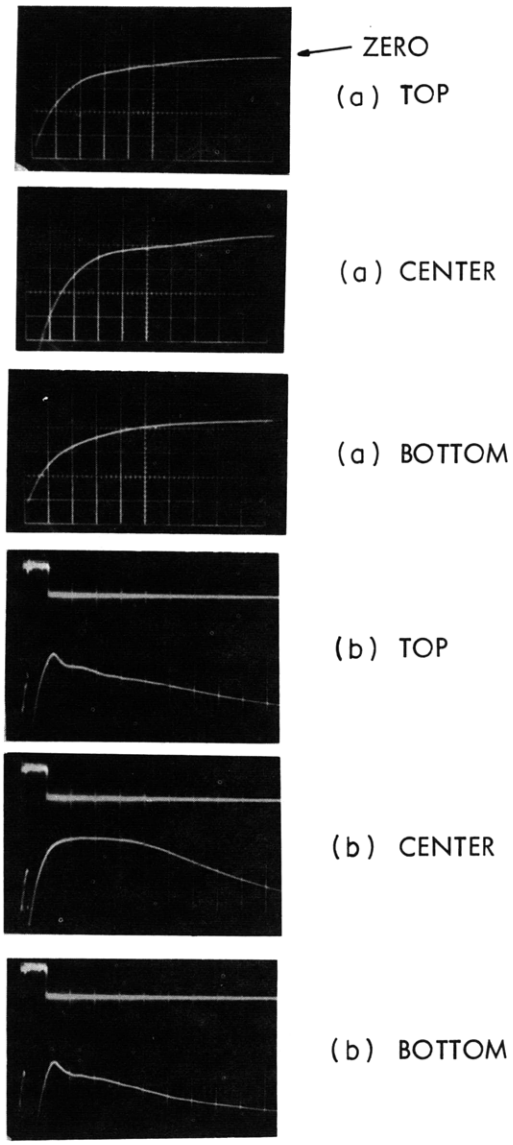

Fig. IX-16.

Asymmetries near the poloidal magnet support. Neutral pressure: 4.3×10^{-5} Torr of Hydrogen. (a) Ion saturation current at wall-loss probes. I_p = 16000 A. I_t = 1000 A. Horizontal scale: 5 μs/div., beginning at t = 10 μs. Upper: LP2 probe. Middle: LP4. Lower: LP5. (b) Plasma floating potential at wall-loss probes. I_p = 6000 A. I_t = 1000 A. Horizontal scale is 10 μs/div., beginning at t = 0. Upper: LP2. Middle: LP4. Lower: LP5.

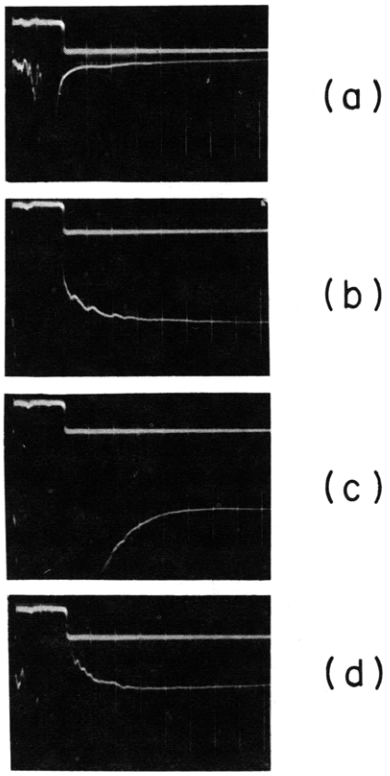

Fig. IX-17.

Plasma oscillations inside of poloidal coil. Horizontal scale is 5 μs/div. I_p = 6000 A. I_t = 1000 A. (a) Ion saturation current for 4.3×10^{-5} Torr of Hydrogen. (b) Double-probe current for a bias voltage of 10 V for 4.3×10^{-5} Torr of Hydrogen. (c) Same as (b) with bias voltage of 30 V. (d) Double-probe current for a bias voltage of 60 V for 4.2×10^{-5} Torr of Argon.

Argon. The drift wave frequency was several hundred kHz.

c. Confinement

The plasma confinement was experimentally determined by analyzing the density decay observed with single and double probes, light emission decay observed with the phototube, ion saturation current decay observed with the wall-loss probes, and the

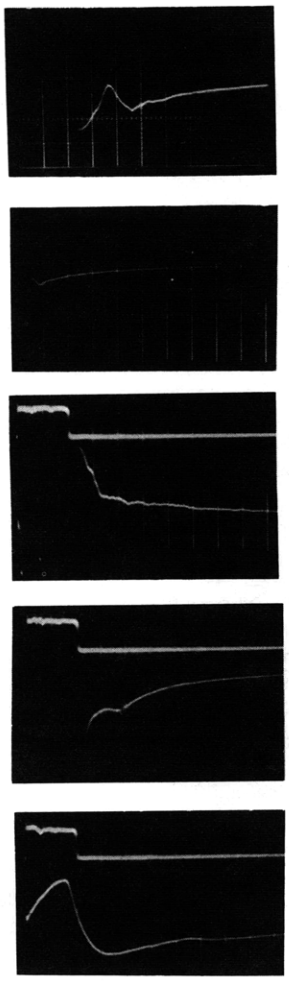

Fig. IX-18.

Changes in decay rates. (a) Ion saturation current out of the plane of the poloidal coil for 6.4×10^{-5} Torr of Hydrogen. I_p = 16000 A. I_t = 4000 A. Horizontal scale is 10 μs/div., beginning at t = 0. (b) Ion saturation current inside of poloidal coil for 4.3×10^{5} Torr of Hydrogen. I_p = 8000 A. I_t = 1000 A. Horizontal scale is 5 μs/div., beginning at t = 0. (c) Double-probe current inside of poloidal coil for a bias voltage of 50 V. I_p = 6000 A. I_t = 1000 A. Horizontal scale is 5 μs/div. (d) Ion saturation current at LP4 wall-loss probe for 8.4×10^{-6} Torr of Argon. I_p = 6000 A. I_t = 1000 A. Horizontal scale is 5 μs/div. (e) Plasma floating potential outside of poloidal coil for 4.3×10^{-5} Torr of Hydrogen. I_p = 6000 A. I_t = 1000 A. Horizontal scale is 5 μs/div. Vertical scale is 10 V/div.

decay of the floating potential. The plasma parameters, particularly the density, slowed their decay rates by approximately a factor of two soon after the end of microwave heating, as seen in Fig. IX-18. The plasma was studied during the second density decay rate and the data are presented in Table IX-1.

The Bohm time of the plasma was given by

$$\tau_b = \Lambda^2\, 16B/(kT_e/e).$$

where Λ is the diffusion length. With a density gradient of ~1.0 cm as the diffusion length, the Bohm time for the Hydrogen plasma at 4.3×10^{-5} Torr was approximately 3 μs. For the Argon and lower pressure Hydrogen plasma with higher electron temperature, the Bohm time was approximately 1 μs.

Table IX-1. Decay times. $I_p = 6000$ A. $I_t = 1000$ A.

	Hydrogen (Torr)		Argon (Torr)	
Diagnostic	4.3×10^{-5}	8.6×10^{-6}	4.2×10^{-5}	8.4×10^{-6}
	(μs)	(μs)	(μs)	(μs)
Density decay: double floating probe	45	30	30	30
Density decay: single probe	27 (a)			
Light emission decay: phototube	67	75	70	55
Ion saturation current decay: wall-loss probes	20 (b)	17		48
Floating potential decay: wall-loss probes	55	55		
Floating potential decay: single probe	100 (c)			
Bohm time	3	1	1	1

(a) $I_p = 15{,}000$ A, $I_t = 4000$ A, $p = 6.4 \times 10^{-5}$ Torr.

(b) $I_p = 12{,}000$ A.

(c) Situated 1.0 cm from the outer radius of the poloidal coil.

If the sole source of particle loss were due to the interception of particle orbits by the poloidal coil support, the plasma decay time would have been: $\tau_s = nV/2(nAv/4)$, where nV is the total number of ions, and nAv/4 was the arrival rate of the slower particle, the ions, at velocity v, onto one side of the support of cross-sectional area A. The average ion arrival velocity was given by $(8kT_e/\pi m_i)^{1/2}$. Thus we find $\tau_s = 30$ μs for Hydrogen at 4.3×10^{-5} Torr.

In view of the magnitudes of the support loss time and of the ion saturation current decay time at the wall-loss probes, the plasma appears to have been lost during heating and immediately thereafter across magnetic field lines to the walls, but after the break in time constants the plasma loss was mainly to the support.

A. S. Ratner, R. A. Blanken

References

1. B. Lehnert, Nature 181, 331 (1958).
2. O. A. Anderson, D. H. Birdsall, C. W. Hartman, E. J. Lauer, and H. P. Furth, "Plasma Confinement in the Levitron," in "Proceedings of a Conference on Plasma Physics and Controlled Nuclear Fusion Research at Novosibirsk, U.S.S.R., 1968" (International Atomic Energy Agency, Vienna, 1969), Vol. 1, p. 443.
3. A. F. Kuckes and R. B. Turner, "Plasma Confinement in a Small Aspect Ratio Levitron," in "Proceedings of a Conference on Plasma Physics and Controlled Nuclear Fusion Research at Novosibirsk, U.S.S.R., 1968," op. cit., Vol. 1, p. 427.
4. S. Yoshikawa, M. Barrault, W. Harries, D. Meade, R. Palladino, and S. von Goeler, "Linear Multipole and Spherator Experiments," in "Proceedings of a Conference on Plasma Physics and Controlled Nuclear Fusion Research at Novosibirsk, U.S.S.R., 1968," op. cit., Vol. 1, p. 403.
5. J. G. Laframboise, "Theory of Spherical and Cylindrical Probes in a Collisionless, Maxwellian Plasma at Rest," UTIAS Report No. 100, University of Toronto Institute for Aerospace Studies, 1966.
6. R. Freeman, M. Okabayashi, H. Pacher, G. Pacher, and S. Yoshikawa, Phys. Rev. Letters 23, 756 (1969).
7. M. Yoshikawa, T. Ohkawa, A. A. Schupp, Phys. Fluids 12, 1926 (1969).
8. S. Yoshikawa, R. Freeman, and M. Okabayashi, "Effect of Neutral Particles and Supports on the Confinement of Plasma in the Spherator," Report MATT-706, Plasma Physics Laboratory, Princeton University, 1969.
9. S. Yoshikawa, "Spherator and Related Experiments," Report MATT-735, Plasma Physics Laboratory, Princeton University, 1969.

2. QUIESCENT RADIOFREQUENCY PLASMA EXPERIMENT

A steady-state collisionless plasma with a low level of turbulence has been generated in a solenoidal geometry using a Lisitano coil. Electron density varies from 0.1 to 2.0×10^{11} cm^{-3}, and electron temperature from 3 eV to 10 eV, depending on the radial position and the coupled RF power. At an operating pressure of 10^{-5} Torr both electrons and ions are collisionless with respect to the neutrals ($\omega_c \tau_{i,en} \gg 1$). For low-frequency long-wavelength instabilities such as drift waves (small $k_{\parallel}$), the high density case is near the electron-ion collisional threshold ($\omega_d \tau_{ei} \approx 1$), while for the lower density case the plasma is collisionless ($\omega_d \tau_{ei} \gg 1$). Low-frequency turbulence (0-30 kHz) is peaked at the plasma edge similarly to edge oscillations found in Q-machines. The amplitude, coherence, and frequency spectrum can be varied to some extent with end-plate biasing. These plasma characteristics are suitable for studying turbulence and transport phenomena.

System

A schematic diagram of the system is shown in Fig. IX-19. It is a modified form of the HCD-III which was used by D. J. Rose and J. C. Woo.[1] The stainless-steel

vacuum can (14.6 cm ID) has been lengthened to 350 cm and two diffusion pumps and magnets have been added. The system can now be operated either as a mirror machine or as a solenoid with magnetic field variable from 0 to 3.5 kG in any section. Since the

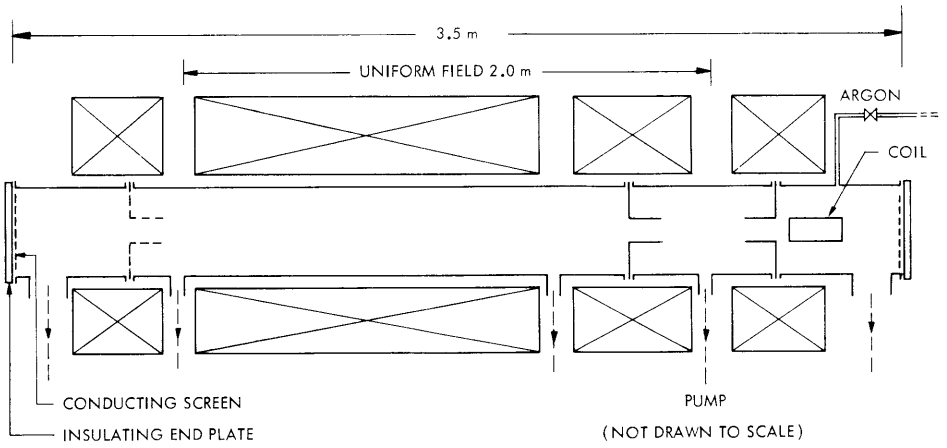

Fig. IX-19. Schematic of the system.

operation of the Lisitano coil is based on electron-cyclotron resonance heating (ECR) the regulation of the mirror fields has been improved to 0.5%. Neutral pressure is controlled with double baffles of 5-cm aperture, and a third baffle can be installed for operation with a coil at the other mirror. Neutrals are introduced into the coil region by a variable flow gas feed and are trapped in the coil region by the baffles.

Coil Design

A schematic diagram of the coil is shown in Fig. IX-20. The design is similar to those used by Lisitano.[2-4] The coil can be visualized as a slotted microwave antenna folded onto a conducting metal cylinder so that the electric field across the slot lies in a plane perpendicular to the coil axis. A conducting cylindrical shield is placed concentrically over the slotted cylinder to prevent outward radial power loss. With the shield installed, power can radiate only as TE or TM modes inside the slotted cylinder. By choosing the radius sufficiently small, these modes are cut off and only an evanescent field can exist in the coil. One end of the slot is made one-quarter wavelength long to isolate the end from the power feed. The rest of the slot, which is folded onto the coil and couples energy into the plasma, is made a nonintegral number of half-wavelengths long to avoid an impedance mismatch where the power is fed into the coil. RF power at 3 GHz is coupled through the shield to the slot as shown in Fig. IX-20. For ECR heating, a 1-kG field in the slot region is necessary. The 0.5% regulation of the magnetic field

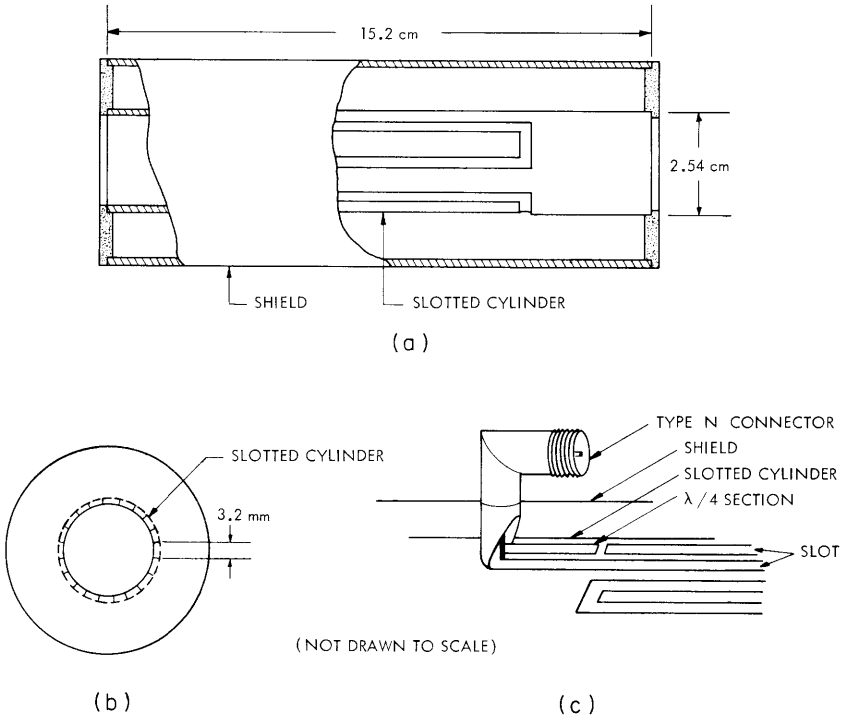

Fig. IX-20. Schematic of the coil.

is sufficient if the coil is operated in a small magnetic field gradient. If the field is too flat, erratic operation is incurred and more regulation is needed.

By constructing the coil with both ends open, magnetic field lines passing through the coil aperture will also pass through the end plates, thereby ensuring good contact between the end plates and the plasma. This was found to be important for turbulence control.

Density is limited by electron shielding of the coil slots. For a resonant magnetic field, this corresponds to the upper hybrid cutoff condition, that is,

$$\omega_p^2 = N(N+1)\ \omega_{ce}^2, \tag{1}$$

where N is the harmonic number ω_{RF}/ω_{ce}. For the first harmonic this corresponds to a density of 2.2×10^{11} cm^{-3}.

An indication of the effect of ECR heating on the electron distribution function can be made by calculating the perpendicular energy gained by an electron making a single pass through the resonance region of the coil. An electron with temperature T at an angle θ_o to the magnetic field will undergo heating for an effective correlation time determined by the temperature, the RF source bandwidth, and the field gradient. The heating width of the resonant region can be related to the source bandwidth and field

gradient as follows:

$$\frac{\Delta f_{RF}}{f_{RF}} = \frac{\Delta B}{B} = \frac{\Delta x}{\lambda_B}, \tag{2}$$

where λ_B is the magnetic field scale length $\left(B/\frac{dB}{dS}\right)$. It follows that the correlation time is

$$\tau = \frac{\Delta x}{v_{||}(\theta_o, T)}, \tag{3}$$

and the change in perpendicular energy of an electron for a single transit through the coil will be (in eV)

$$\Delta W(T, \theta_o) = E_\perp v_\perp(\theta_o, T)\, \tau + \frac{eE_\perp^2}{2m}\tau^2. \tag{4}$$

For the magnetic field, slot width, and applied power used in our system, a typical electron will receive the energy change (in eV)

$$\Delta W(T, \theta_o) \approx \tan \theta_o + \frac{1}{2T(\cos \theta_o)^2} \tag{5}$$

which is plotted in Fig. IX-21.

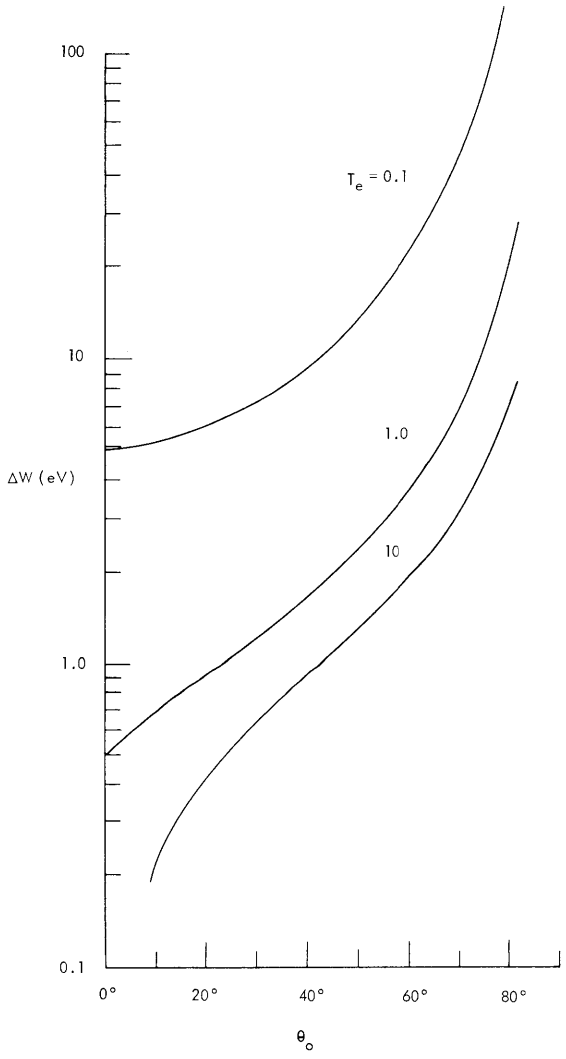

Fig. IX-21. ΔW vs θ_o for various electron temperatures.

It follows from Fig. IX-21 that the energy gained is only a few eV for a typical particle, while a small population of electrons receive over 100 eV. Since the ion saturation current collected by a cold spherical probe is several orders of magnitude less than electron saturation current, these hot electrons may introduce errors in floating-potential measurements. For our plasma, this population should be small, since electrons are axially trapped in the plasma column by the sheaths at the end plates. The hottest electrons should scatter in angle off the background neutrals and escape through the end sheaths. All particles will scatter in angle off the neutrals, but only the very hot electrons can

pass through the sheath potential. Since the ions migrate slowly to the end sheaths, the electrons are contained for a period much longer than the electron-electron thermalization time. It is concluded that most electrons that are trapped in the column should have a Maxwellian distribution. This was verified with probe characteristic curves. At low density, however, where the thermalization time is long, current collecting probes had to be biased at ϕ probe/$T_e \approx 20$ to obtain good results for ion saturation current.

Plasma Properties

A cylindrical plasma column, 350 cm long and 3-4 cm in diameter, was formed by coupling 3-20 W of RF power to the plasma. The gas was Argon at a pressure of $3\text{-}7 \times 10^{-4}$ Torr in the coil region and $0.6\text{-}1.5 \times 10^{-5}$ Torr in the baffled region. For these pressure ranges, the general properties were insensitive to small changes in neutral pressure. By varying the coupled power to the plasma (incident minus reflected power) the density was varied over an order of magnitude as shown in Fig. IX-22.

Spherical probes with a radius of 0.57 mm were used to measure density and temperature. Since the ion Larmor radius is much larger than the probe radius, collisionless probe theory was used.[6,7]

A typical density profile is shown in Fig. IX-23 for 12 W of power coupled to the plasma. The radial density profile was found to be insensitive to coupled power and changed only in magnitude. The profile appears to be radially limited by the coil inner radius (1.25 cm).

Electron temperatures for 12 W and 5 W power yield similar radial profiles (Figs. IX-24 and IX-25); however, more efficient electron-ion thermalization at higher densities results in a lower electron temperature for 12 W. The ion temperature is sensitive to the ratio of electron-to-neutral density and is expected to be approximately 0.4 eV for our experiment.[5] It is of interest that electron temperature and density gradients are opposed out to a radius of 0.75 cm; however, coherent oscillations indicating an instability in this region were not observed.

Plasma Turbulence

Broadband low-frequency turbulence and coherent modes have been observed.

Broadband low-frequency turbulence (0-30 kHz) appears at all radii but has a maximum at the plasma edge. On the column axis it is only a few percent as shown in Fig. IX-26, but increases to over 10% near the inner radius of the coil. Beyond a radius of 1.25 cm, the plasma becomes fully turbulent and probe measurements indicate a "flutelike" motion of the plasma. Figure IX-27a shows the spectrum 0-100 kHz of log (Δn) and Fig. IX-26 shows the radial dependence. This condition is found at all

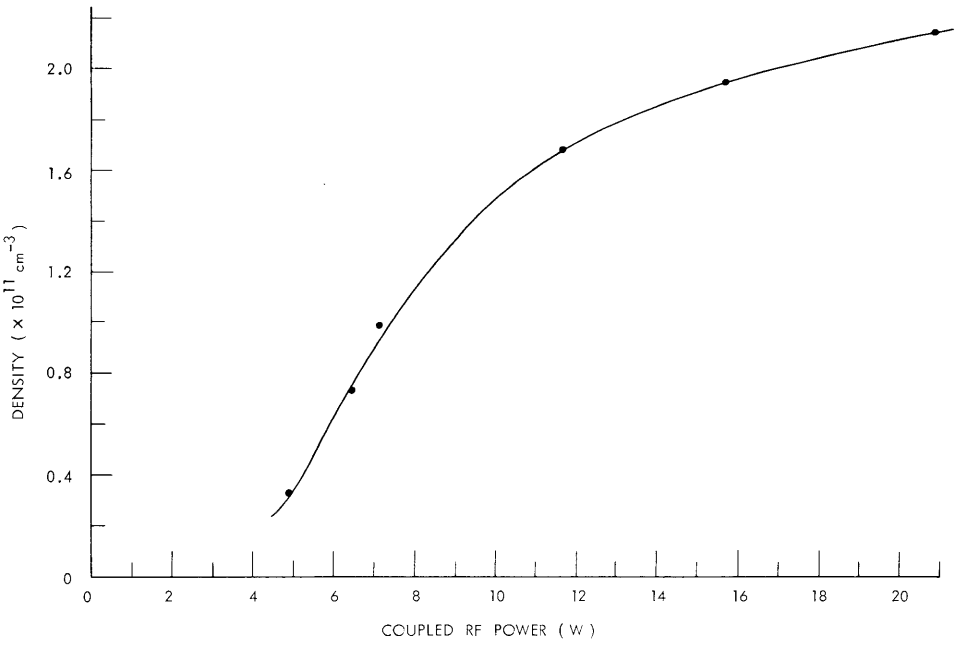

Fig. IX-22. Electron density vs coupled power.

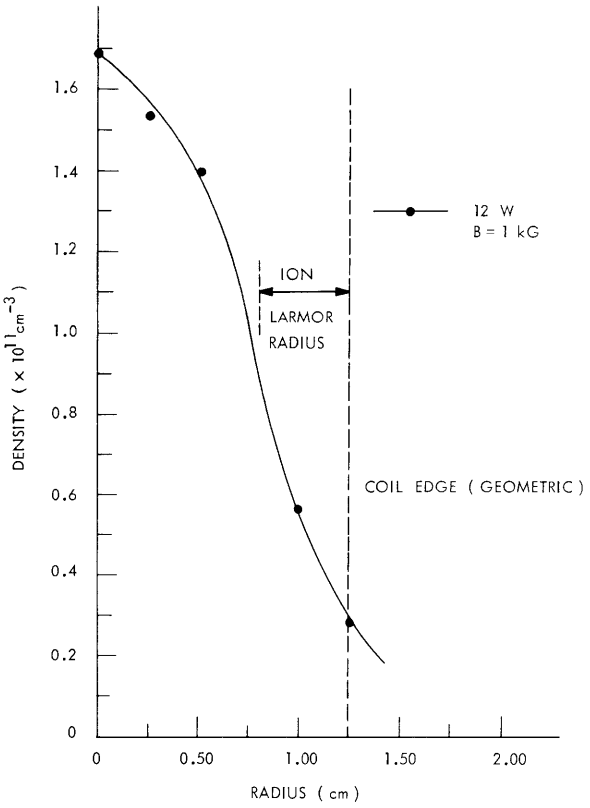

Fig. IX-23. Electron density vs radius.

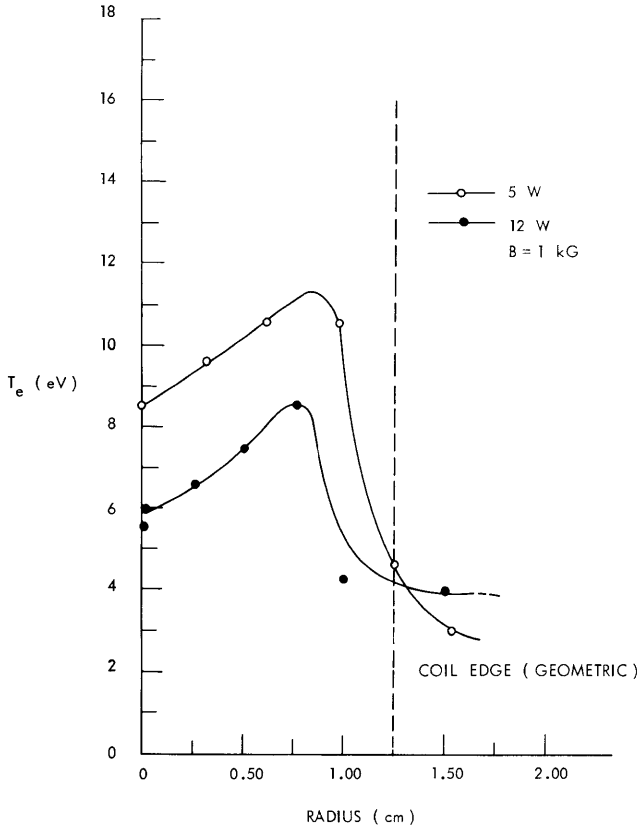

Fig. IX-24.
Electron temperature vs radius.

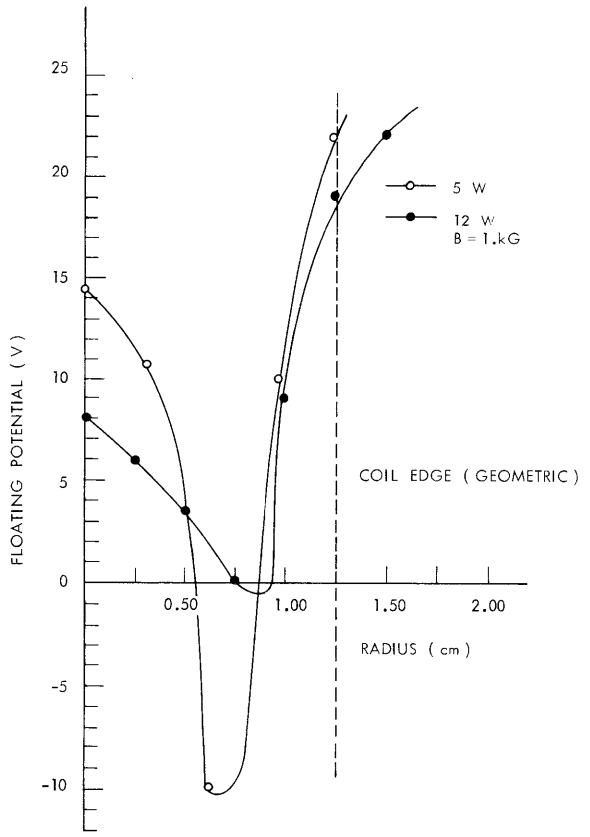

Fig. IX-25.
Floating potential vs radius.

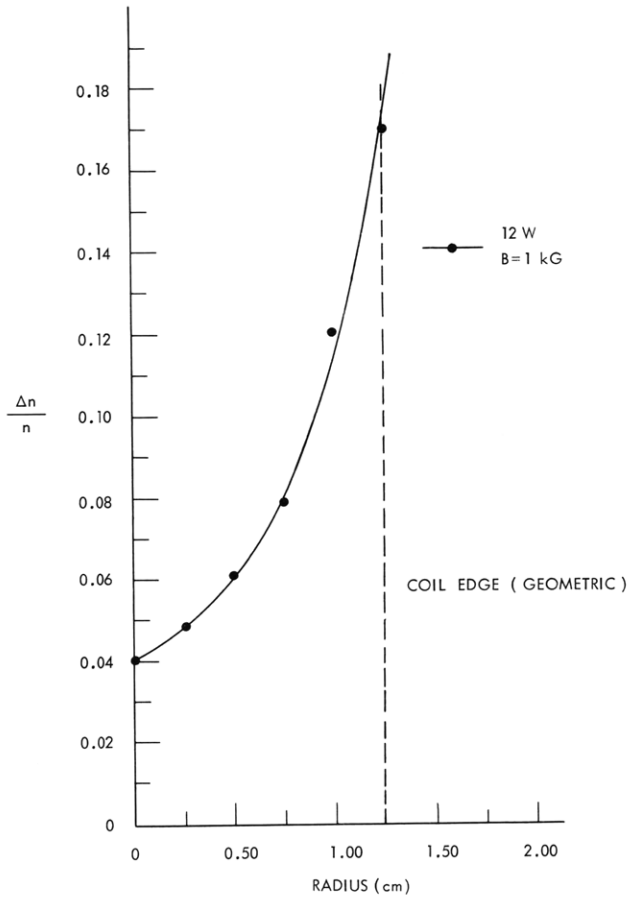

Fig. IX-26. Δn/n vs radius, rms.

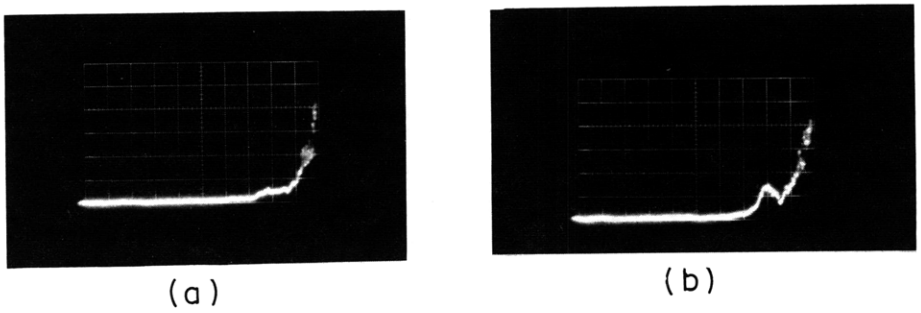

Fig. IX-27. Δn, 100-0 kHz, log-uncalibrated: (a) r = 0; (b) r = 1.5 cm.

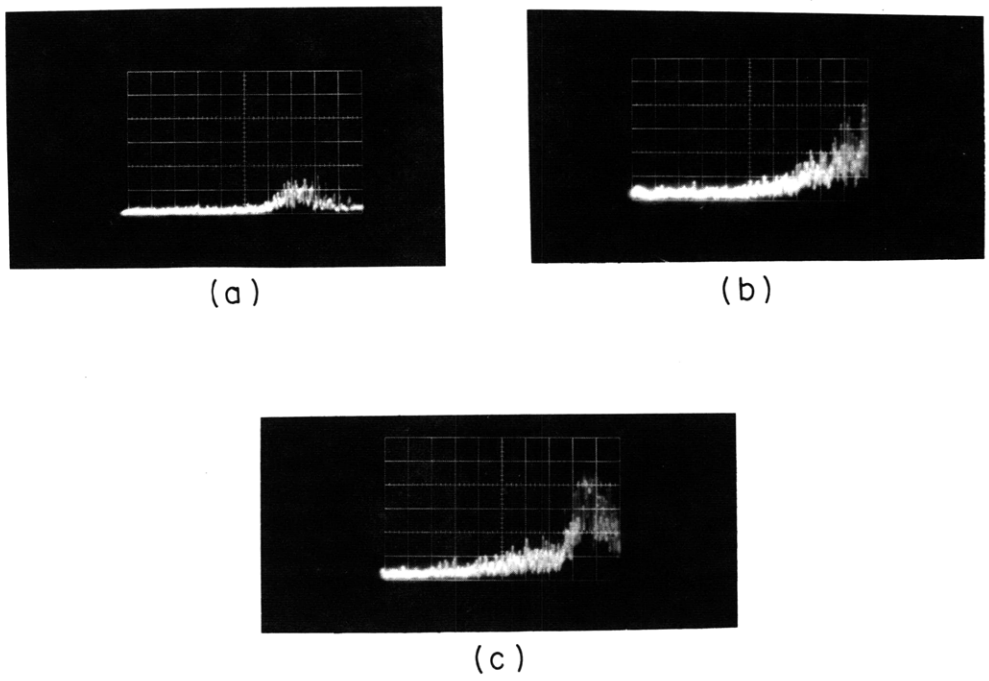

Fig. IX-28. Δn, 12-2 kHz, rms: (a) +20 V end-plate biasing; (b) 0 V; (c) -20 V.

operating densities and resembles edge oscillations found in Q-machines.[8] Figure IX-28 shows how this spectrum can be controlled by end-plate biasing. The photographs show the degree of control over Δn, 2-12 kHz. It is possible to turn on or off a coherent mode near 4 kHz by properly biasing the end plates. Since density and temperature gradients are small and the radial electric field is large near the edge, the turbulence may be a Rayleigh-Taylor flute or a Kelvin-Helmholtz instability driven by the radial electric field. The dependence upon end-plate biasing supports the theory that the waves are driven by the radial electric field. The flutes appear to be m = 1 modes.

For densities greater than 10^{11} cm^{-3} a coherent wave was observed centered at a radius of 1.5 cm. This also appears in a region where density and temperature gradients are small. Figure IX-27b shows this wave.

J. E. Robinson, E. Oktay, L. M. Lidsky, R. A. Blanken

References

1. J. C. Woo, Sc.D. Thesis, Department of Nuclear Engineering, M.I.T., June 1966.
2. G. Lisitano, R. A. Ellis, W. M. Hooke, and T. H. Stix, Report MATT-Q-24, Plasma Physics Laboratory, Princeton University, 1966.
3. G. Lisitano, private communication (1969).
4. P. Politzer, private communication (1969).

5. M. Hudis, K. Chung, and D. J. Rose, J. Appl. Phys. 39, 3297 (1968).

6. J. G. Laframboise, Report 100 University of Toronto, Institute for Aerospace Studies, 1966.

7. F. F. Chen, C. Etievant, and D. Mosher, Phys. Fluids 11, 811 (1968).

8. D. L. Jassby and F. W. Perkins, Phys. Rev. Letters 24, 256 (1970).